PHYSICAL REVIEW D VOLUME 53, NUMBER 8 15 APRIL 1996

Event horizons in numerical relativity: Methods and tests

Joseph Libson,[1,3] Joan Massó,[1,2] Edward Seidel,[1,3] Wai-Mo Suen,[4] and Paul Walker[1,3]
[1]*National Center for Supercomputing Applications, Beckman Institute, 405 N. Mathews Avenue, Urbana, Illinois 61801*
[2]*Departament de Física, Universitat de les Illes Balears, E-07071 Palma de Mallorca, Spain*
[3]*Department of Physics, University of Illinois, Urbana, Illinois 61801*
[4]*McDonnell Center for the Space Sciences, Department of Physics, Washington University, St. Louis, Missouri 63130*

(Received 30 November 1994; revised manuscript received 11 September 1995)

This is the first paper in a series on event horizons in numerical relativity. In this paper we present methods for obtaining the location of an event horizon in a numerically generated spacetime. The location of an event horizon is determined based on two key ideas: (1) integrating backward in time and (2) integrating the whole horizon surface. The accuracy, efficiency and robustness of the methods are examined with various sample spacetimes, including both analytic (Schwarzschild and Kerr) and numerically generated black holes. The numerically evolved spacetimes contain highly distorted black holes, rotating black holes, and colliding black holes. In all cases studied, our methods can find event horizons to within a very small fraction of a grid zone.

PACS number(s): 04.25.Dm, 04.70.−s, 97.60.Lf

I. INTRODUCTION

Black holes are among the most fascinating predictions in the theory of general relativity. During the past 20 years there have been intense research efforts on black holes and their effect on the astrophysical environment. With the exciting possibility of detecting gravitational wave signals from black holes by the gravitational wave observatories under construction [the Laser Interferometric Gravitational Wave Observatory (LIGO) and VIRGO [1]], we have seen an increasing surge of interest. The black hole events likely to be observed by the gravitational wave observatories involve highly dynamical black holes, e.g., two black holes in collision. The most powerful tool in studying such highly dynamical and intrinsically nonlinear events is probably numerical treatment. In recent years, there has been significant progress in numerical relativity in this direction (see, e.g., Refs. [2,3]). In particular, long evolutions of highly dynamical black hole spacetimes are now possible [4,5], opening up the opportunity of many interesting studies.

The defining character of a black hole is its event horizon (EH). The EH is defined as the boundary of the causal past of the future null infinity (for a rigorous description, see, e.g., Ref. [6]). Photons emitted inside this boundary surface cannot escape to infinity while those emitted outside in a suitable direction can. It is the existence of such a boundary surface that makes a black hole ‘‘black.’’ Only when a horizon surface is located can we know for sure that the spacetime that we are studying contains a black hole.

Locating such horizon surfaces is the subject of this first paper in our series studying event horizons in numerical relativity. Event horizons can now be found in numerically generated spacetimes, and their dynamics can be traced out, using methods we outlined in Ref. [7]. These methods were also used to generate and study event horizons for two colliding black hole spacetimes in Ref. [8]. In another example, the first case of a toroidal black hole event horizon was discussed in Ref. [9]. The present paper provides details of the methods needed to find the event horizon in numerically generated spacetimes.

The study of the dynamics of this surface is crucial for understanding the dynamics of a black hole spacetime. In the membrane paradigm of black holes [10], black holes are characterized by the properties of its EH, which is regarded as a two-dimensional (2D) membrane living in a 3D space, evolving in time and endowed with many everyday physical properties like viscosity, conductivity, entropy, etc. We believe this point of view is powerful in providing insight into the numerical studies of black holes. In the second paper in this series [11], we present methods and tools for studying these properties of the horizon surface. In the third paper in the series [12], we turn to the physics of black holes that can be explored using these tools.

There are two properties of the EH that make its location difficult to determine in numerical relativity: It is defined nonlocally both in space and in time and, moreover, in an acausal manner. Therefore its location, and even its existence, at any time cannot be determined without knowledge of the complete four-geometry of the spacetime. We will demonstrate how to overcome these difficulties.

Consider a numerically constructed spacetime represented by a set of data given on a 3+1 lattice. Suppose the numerical evolution has covered a region of spacetime so that at the end of the evolution one can locate a spatial domain which is likely to contain the EH. (We show below how this can be done.) On the one hand, as numerical evolution often does not cover null infinity [13], generally one cannot give a precise location of the EH even on the final time slice. On the other hand, the black hole events we are interested in often involve black holes eventually settling down to a stationary state after going through violent processes, e.g., the coalescence of two black holes. If the numerical evolution covers late enough times, so that at the end of the evolution the geometry returns approximately to stationarity, it is often easy to have an *approximate* location of the EH, as we shall show below. We note that at late times, if the spacetime has truly returned to stationarity, the difficulties of finding the EH due to its acausal nature and nonlocality in time disappear, as the geometry is the same on each time slice henceforth.

Of course, true stationarity is probably impossible in numerical evolution. One can aim at most at approximate stationarity. We note that such approximate stationarity is possible, as dynamical black hole spacetimes can now be evolved for a long time (commonly $t \approx 100M$, and in some cases to $1000M$) [14–16]. Therefore the first set of questions in the numerical study of black hole EH's is the following.

Consider a numerically constructed spacetime, such that one has an approximately stationary final configuration. Assume that although the EH cannot be located exactly, it is known to exist in a certain spatial domain. Can one determine this horizon-containing domain in all the previous time slices during which the spacetime is highly dynamical, which is often the real epoch of interest? That is, how does this horizon-containing domain evolve in a dynamical spacetime? We will show that in the language used here, even if the horizon-containing domain is fairly large at the final time, it can be narrowed down tremendously at earlier times. This is true not only for analytic spacetimes, but also for dynamical ones. If the EH can be approximately located at late times, after the black hole and surrounding spacetime return to approximate stationarity, we show that the EH can be accurately determined throughout the dynamical period of interest.

The present paper focuses on this set of problems of locating the EH in a black hole spacetime. We have developed two generations of ''event horizon finders,'' based on two basic ideas [7]: (1) Integrate backward in time, and (2) integrate the horizon surface instead of the individual geodesics. We discuss these ideas in detail in Sec. II. In Sec. IV we examine how much accuracy one can obtain in locating the EH throughout its history (i.e., how small the horizon-containing domain can become) in various sample numerically constructed spacetimes, including distorted Schwarzschild and Kerr black holes, and colliding black holes. We also compare various methods for locating the EH, including our two generations of EH finders based on backward integration and another method recently proposed using forward integration [9].

A basic assumption in this paper is that one can locate a certain horizon-containing domain at the end of the numerical evolution. An interesting question is to what extent one can use the techniques developed in this paper to improve confidence that the domain truly contains an EH or to rule out such a possibility. Although we shall not deal with this question in this paper, it is easy to see that the techniques developed can also be useful in this regard. In Sec. IV we shall see that one can easily narrow this domain on the final configuration to a large extent by examining trajectories of null surfaces.

II. METHODS

Suppose for the moment that the actual event horizon (EH) is given on the final time slice of the numerical evolution (for simplicity of discussion, the evolution is assumed to be in the 3+1 slicing of spacetime; other schemes, such as 2+2, could be treated as well). How does one determine its location at earlier times? One may consider integrating null geodesics forward in time, selecting those that successfully arrive at the given EH at the final time. There are two conditions that must be satisfied for success: (i) The geodesic must land on the given EH, and (ii) the tangent of the geodesics must be the outgoing normal to the EH. In principle, such stringent requirements could be satisfied and the history of the EH could be traced out with such an algorithm. However, there is an intrinsic difficulty, making such an algorithm very inefficient. By the definition of the EH, outgoing null geodesics slightly inside the EH will fall into the singularity after some short time, while outgoing null geodesics just slightly outside will escape to null infinity. Therefore, evolving null geodesics forward in time near the EH is a physically unstable process.

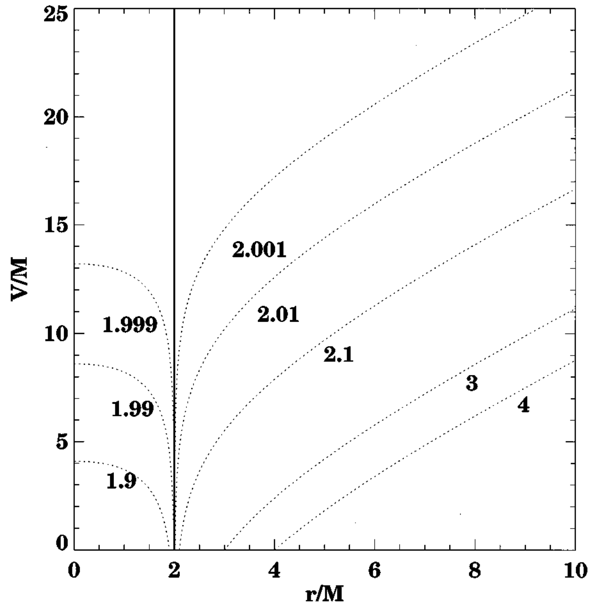

FIG. 1. A spherical black hole spacetime is shown in Eddington-Finkelstein coordinates with several outgoing null rays trajectories plotted. The horizon is shown as a solid line, while various photon paths are shown as dotted lines, with their r/M location marked.

In Fig. 1 the behavior of various outgoing null geodesics in a spherical black hole spacetime is shown in terms of Eddington-Finkelstein coordinates [17]. The horizon is given as a solid line while photons are given as dotted lines. Outgoing null geodesics starting out infinitesimally close to the horizon spread out to cover a large region of the spacetime. They are ''everywhere'' on a late time slice. This physical instability, coupled with the inevitable finite differencing error in a numerical calculation, ensures that null geodesics will move away from the true position of the EH, even if they are right on it initially. An accurate determination of the history of the EH will not be possible unless (a) the spacetime data have a very high resolution, and (b) a very large number of photons is followed, so that they are ''dense'' enough to have some of them stay near the EH throughout the evolution.

However, a moment's reflection tells us that this important property of the EH can be used to our advantage; the instability of integrating outgoing null geodesics forward in time near the EH implies that when integrating these geodesics backward in time near the EH, they will converge onto the horizon. The backward direction is the stable direction of integration. This is one of the two basic ingredients in building our EH finders. In our first generator EH finder [18,19], called the "backward photon" method, we trace the EH by integrating null geodesics backward in time. The geodesic equation is a second order differential equation,

$$\frac{d^2x^\alpha}{d\lambda^2} = -\Gamma^\alpha{}_{\beta\gamma}\frac{dx^\beta}{d\lambda}\frac{dx^\gamma}{d\lambda}, \tag{1}$$

where λ is an affine parameter along the geodesic.

We note that this backward integration method requires that one first complete the spacetime evolution and store the entire spacetime evolution metric, or at least a strip of it which safely contains the full history of the EH. However, in all cases we studied, being able to integrate in the stable direction is well worth the extra storage requirement. As the null geodesics are "attracted" to the EH when integrated backward, we found that the position of the EH can be determined to an accuracy of a small fraction of a grid zone, as shown in the next section. (Forward integration schemes generally also require storing the entire spacetime evolution, as many photons must be "shot" forward and then tested to see if they end up inside or outside the horizon at the final time [9].)

Two comments regarding the "attraction" of the EH in backward integration are in order. First, this "attraction" is only in the global sense. Locally, the EH has no special property. That is, geometrically the EH is not distinct from other surfaces. As the geodesic deviation equation is governed by the Riemann curvature tensor, which has no special value at the horizon, the outgoing null geodesics are not attracted to the EH in any local sense. On the other hand, in a 3+1 numerical evolution, only those outgoing null geodesics that are either very near or inside the EH at early times can remain in the finite range of the spacetime with a nonvanishing lapse which is covered by the numerical evolution at late enough times. In other words, when integrating backward in time, outgoing photons in this range approach the EH after a sufficiently long integration. The EH is attractive only in this global sense in time. Note that this attractive property implies that our starting point in the backward integration need *not* be exactly on the EH. This is a key point that we will quantify below.

Second, this attractive property of the horizon is just for outgoing photons. An ingoing photon when traced backward will not only leave the EH surface; it may even leave the finite region of the spacetime. In the one-dimensional case, inward and outward photons are clearly distinct (only outgoing ones are displayed in Fig. 1), but for the general 3D case, when the two tangential directions of the EH are also considered, the situation becomes more complicated. (Here normal and tangential are meant in the 3D spatial, not spacetime, sense.) Whether or not a trajectory can eventually be "attracted" to the EH, and how long it takes for it to become "attracted," depends on the photon's starting direction of motion. We note that even for a photon which is already exactly on the EH at a certain instant, if its velocity at that point has some component tangential to the EH surface (as generated by, say, numerical inaccuracy in integration), the photon will move outside of the EH when traced backward in time. For a small tangential velocity, the photon will eventually return to the EH. The duration and distance it moves outside the EH depend on its tangential velocity. Also, the position to which it returns will not be the original position.

This kind of tangential drifting is undesirable not just because it introduces inaccuracy in the location of the EH, but more importantly, because it can lead to spurious dynamics of the "EH" thus found. Neighboring generators may cross, leading to numerically artificial caustic points (for an introductory discussion of caustics, see, e.g., Ref. [17], Chap. 10).

Unfortunately such tangential drifting is not easy to avoid due to the nature of the geodesic equation (1) which we integrate backward. The geodesic equation is not only second order, but also requires derivatives of the numerically generated metric data which are generally more inaccurate.

Another consequence of the second order nature of the geodesic equation is that not just the positions but also the directions must be specified in starting the backward integration. Neighboring photons must have their starting direction well correlated in order to avoid tangential drifting across one another. We find it important to make explicit use of the property that the surface we wish to trace is a closed 2D surface embedded in 3D space at the start of the backward integration. While the starting positions of the photons are taken to be on this surface, the starting directions are taken to be normals to this surface. Of course even if the geodesics have accurate starting values they may still drift due to inaccuracy in integration, as discussed above. We find that the "backward photon" method is still quite demanding in finding an accurate history of the EH, although the difficulties are much milder than those arising from the instability of integrating forward in time.

In our second generation horizon finder, building on the above idea of explicitly using the surface-forming property of the EH, we follow the entire horizon surface itself, rather than tracking individual photons independently. Generally speaking, the EH can be considered as a 2+1 null surface, except at special points where its normal cannot be defined. Except for these special points, which we shall discuss later, one can represent the 2+1 EH surface by a function

$$f(t,x^i)=0, \tag{2}$$

which satisfies the null condition

$$g^{\mu\nu}\partial_\mu f\partial_\nu f=0. \tag{3}$$

Hence the evolution of the surface can be obtained by a simple integration:

$$\partial_t f=\frac{-g^{ti}\partial_i f+\sqrt{(g^{ti}\partial_i f)^2-g^{tt}g^{ij}\partial_i f\partial_j f}}{g^{tt}}. \tag{4}$$

In our second generation horizon finder, we integrate this equation backwards in time. This is what we call our "backward surface" method. Notice that at the final time, the EH is given as a closed 2D surface. Given this as the starting condition for the backward integration of Eq. (4), there is no other condition needed (e.g., there is no need to specify either an initial direction or boundary conditions for the surface). The reconstruction of the complete function $f(t,x^i)$ gives us the full history of the EH (in fact, much more than this, as we will discuss below and detail in Ref. [11]).

Both the backward photon and backward surface method work very well as shown in Sec. III below. However, there is a number of advantages of using the backward surface method.

(i) Of primary importance is that the method is simpler and less susceptible to numerical error than the backward photon method. Notice that Eq. (4) contains only derivatives of the surface and *not* of the metric components themselves and is therefore less susceptible to the numerical inaccuracies present in the metric data. The horizon is generally found in numerically evolved spacetimes in regions where metric functions contain rather steep gradients that are poorly resolved [20], and hence their derivatives may not be accurately known there.

(ii) Tangential drifting is not a source of error, because the only direction that a surface can move is normal to itself. Once the surface becomes the EH, it cannot drift away from it. This is in contrast to integrating geodesics; even if the geodesic is right on the horizon at some instant in time, it does not guarantee that it can stay on it all the time. See Fig. 3 below.

(iii) Unlike integrating null geodesics, the result of this method is guaranteed to be surface forming, as we are explicitly integrating surfaces. This is a nontrivial advantage over integrating geodesics; in particular, the integrated geodesics can fail to be surface forming, either due to the numerical error discussed above, or due to the existence of caustics on the horizon. At the caustics the geodesics leave the EH surface when integrated backward in time. If there are geodesics leaving the EH through caustics, but this caustic point is not so recognized, and the EH is taken to be the surface connecting all geodesics, the evolution history of it would be completely wrong. However, it is nontrivial to determine whether a caustic or numerical error causes geodesics to become non surface forming. In both cases, we may see null geodesics cross one another and move outward. See Fig. 3 below.

(iv) The surface method is naturally suitable for handling and studying caustic structures on the EH. (Here for simplicity of discussion we indiscriminately refer to all classes of points at which horizon generators leave the EH when traced backward in time as horizon caustics; see, e.g., Ref. [17].) As the normals of the EH are different when the caustic point is approached in different directions, strictly speaking the EH is not a null surface at such points, and Eq. (4) would seem to be in difficulty. However, we note that in the generic case of an isolated caustic point, the EH surface surrounding the caustic point can be evolved using one-sided spatial derivatives on the right-hand side (RHS) of Eq. (4). Despite the fact that there is no well defined normal to the surface at a caustic, the motions of surface elements on different sides of the caustic must be continuous as determined by Eq. (4) with appropriate one sided derivatives, as the EH is a continuous closed surface at each time slice. In the two-black-hole collision case studied below in Sec. IV D, Fig. 10, there is clearly a cusp in the EH along the z axis, so that the surface is not smooth there, but it is continuous. This is obtained with a one-sided treatment of the derivative there. This treatment requires knowledge of where caustics would be forming *a priori*. Such *a priori* knowledge is often possible for spacetimes with symmetry properties. In fact, all dynamic black hole spacetimes evolved to date (of which we are aware) have such properties. At those points where caustics may appear, suitable one-sided derivatives are used.

Alternatively, one can treat horizon caustics with the surface method *without* introducing a special treatment for possible caustic points, provided that we do not restrict Eq. (4) to describe *only* the EH, but *also* the locus of the null generators which leave the EH through the caustic points backward in time. That is, in tracing Eq. (4) backward, we allow the closed surface to cross itself. The point of crossing is the caustic. Although the normal of the surface is not continuous going across the caustic on the EH, it is continuous going from the EH across the caustic point to the locus of generators which has left the EH [21]. This is true provided a suitable identification of neighboring surface elements is used, namely, when the identification of two neighboring surface elements does not change in time. This issue is considered in this paper where we treat the collision of two black holes in Sec. IV D, when caustics are important.

These backward surface and photon methods bring for the first time the possibility of studying the properties of horizon generators and caustics in numerical relativity, but the surface method provides a particularly elegant, economical, and accurate way of computing this structure.

Before we go on to the next subsections on the tests and the accuracy of the methods, we comment on the fact that the starting position of the EH in the backward integration is often not known precisely. As pointed out earlier, as long as the numerical evolution can be carried to a point that the black hole returns to approximate stationarity, it is often possible to locate a region which contains the EH. For example, the apparent horizon (AH) is always inside the event horizon (provided quantum effects are ignored). If an AH is found, it can be taken to be the inner boundary of this horizon-containing region. The real task in locating the horizon is to determine the evolution of this horizon-containing region. Because of the attractive nature of the null surfaces to the EH, the horizon-containing region can be narrowed substantially in the backward integration. Indeed we shall see that, using our methods, it is often easy to narrow this region down to much less than a grid separation used in the numerical construction of the spacetime. In some sense the location of the EH is determined to a precision higher than the resolution of the background spacetime, something seemingly impossible at first sight. This is not paradoxical as in all cases studied in this paper, the EH surface expressed as a function, Eq. (2), is constructed using information and interpolations involving many data points, hence ‘‘washing out’’ some local fluctuations. However, if the horizon-containing region were to just span a few angular grid points, the localization of it to a small fraction of a grid separation would no longer be meaningful.

Using our backward methods we are able to trace accurately the entire history of the EH, as we detail in the next section. However, there are cases in which a region of the numerically constructed spacetime is badly resolved (e.g., the crotch region in the two black hole case study below), where the backward surface method method is capable of producing more reliable results. The basic difference in the two methods is in their computational requirements and convenience. A typical case studied here is that of a black hole interacting with a gravitational wave. Such a case is resolved on a grid of 200 radial by 53 angular zones, and evolved to $t=75M$. To trace the EH to 1/10 of a grid separation for the dynamical period of the evolution $(0M<t<48M)$ takes only a few minutes on a computer workstation. For the backward photon method to achieve the same accuracy, it takes several times longer. For future applications with dynamical black hole spacetimes evolved to thousands of M, we believe the backward surface method is most promising.

III. NUMERICAL TECHNIQUES AND TESTS OF METHODS

In this section we discuss both the numerical implementations of our surface methods and provide examples of their applications to dynamical spherical black holes, distorted axisymmetric black holes with and without rotation, and colliding black holes.

A. Numerical implementations

In the surface method, the location of the surface is represented by a function. The use of a suitable parametrization of the surface is important. For the axisymmetric cases discussed in this paper, a convenient choice is

$$f(t,r,\theta)=r-s(\theta,t)=0. \tag{5}$$

With this parametrization, Eq. (4) for the evolution of the surface becomes

$$\partial_t s=-\frac{-g^{tr}+g^{t\theta}\partial_\theta s+\sqrt{(g^{tr}-g^{t\theta}\partial_\theta s)^2-g^{tt}[g^{rr}-2g^{r\theta}\partial_\theta s+g^{\theta\theta}(\partial_\theta s)^2]}}{g^{tt}}. \tag{6}$$

We will use this as our definition of f for almost every case in this paper.

Next we discuss details of the numerical implementation of these methods. For the backward photon method, we use a standard adaptive step size, fourth order in time Runge-Kutta method [22] to integrate the second order geodesic equation (1). For the surface method we have used a number of methods, including second order leapfrog, a second order MacCormack predictor corrector method, and a fourth order Runge-Kutta method using the method of lines to integrate hyperbolic Eq. (4) in time as a set of coupled ordinary differential equations. All methods give similar results.

In following the horizon backward through the spacetime, we necessarily require a spacetime data at points that do not lie on the numerical grid. For this we must interpolate the spacetime data to the actual location of the horizon at each time. For the backward photon method, we must interpolate *both* the metric and its derivatives to these locations. On the other hand, for the surface method we need *only* the metric itself. For both methods, we find that second order interpolation is adequate to determine these data values.

The angular derivatives of the function $s(t,\theta)$ in Eq. (4) are computed using both second and fourth order finite difference methods, with similar results. Although this way of representing the surface works well for almost all cases discussed in this paper, as we show in Sec. IV D, other parametrizations can be necessary at times.

B. Test beds

1. Spherical black holes

In this section we show how the methods detailed above can be applied to pure, spherical Schwarzschild black holes. We consider both the analytic Schwarzschild solution and a maximally sliced Schwarzschild black hole evolved with the 2D, axisymmetric black hole code described in Refs. [23,14]. We use this important test bed case to show the accuracy to which one can determine the location of the horizon in a numerically evolved spacetime. Although the numerical spacetime is geometrically the static Schwarzschild spacetime, it is evolved with a maximal slicing condition which makes the metric functions change in time. As discussed in Ref. [20], such a time dependence makes even the Schwarzschild spacetime quite difficult to evolve numerically for long periods of time (beyond about $t=100M$ with reasonable grid parameters). As the coordinates fall in towards the hole the horizon moves out in coordinate space, the lapse collapses, and large gradients develop in the metric function near the horizon. (For more details on these problems, see Refs. [20,14].) The advantage of using this as our first test bed case is that, on the one hand, the numerical spacetime constructed with this code has many of the properties and difficulties of a general numerically constructed black hole spacetime. On the other hand, the spacetime is really a Schwarzschild spacetime for which we know where the EH should be for all time. In particular, in the numerical case the apparent horizon (AH) and EH coincide. We have accurate AH finders [24] that can locate the AH and thus, in this case, the EH; on any given single slice of the spacetime we know both horizons without needing to know the future or past of that slice. In the analytic spacetime, the horizon is at $r=2M$. This provides us with important accuracy checks on our methods of locating the EH throughout the evolution.

In Figs. 2(a)–2(d) we show results for a spherical black hole spacetime. For the numerical spacetime in Figs. 2(a), 2(b), and 2(d) we apply our horizon finder to the data obtained in the evolution assuming neither spherical symmetry nor the fact that the spacetime geometry is really Schwarzschild. At the final time slice, the horizon-containing region is determined by examining the lapse function and the radial metric function. For a spacetime evolved with maximal slicing, the event horizon resides in a region with a partially collapsed lapse function. In Fig. 2(a), we show the lapse function α at the final time slice $t=100M$. We take the horizon-containing region to extend from $\alpha=0.1$ to

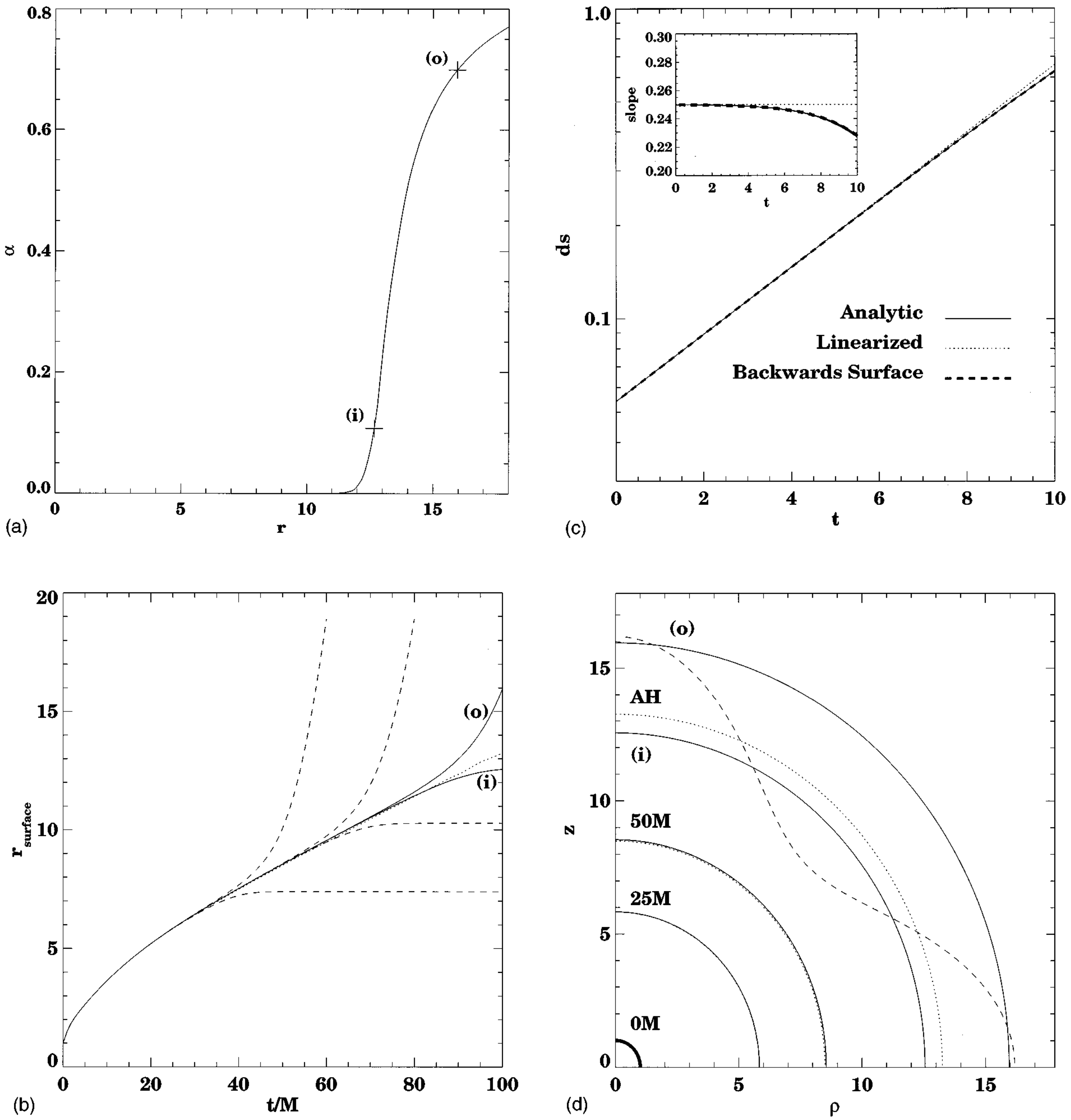

FIG. 2. (a) We show the lapse at $t=100M$ for a single Schwarzschild black hole evolved with our 2D axisymmetric code using maximal slicing. The horizon-containing region, determined by the condition $0.1<\alpha<0.7$, is marked by crosses. The outer edge of the region is marked (o) and the inner is marked (i). (b) We show the evolution of radial coordinate location r of the apparent horizon (dotted line), and the location of horizon-containing region (solid lines) for the backward surface method applied to a Schwarzschild spacetime evolved with our axisymmetric black hole code. The coordinate r equals the isotropic Schwarzschild coordinate at $t=0$. As the evolution continues, the relation between r and the isotropic coordinate becomes a function of the metric. Other test surfaces are shown as dashed lines. All surfaces converge rapidly towards the true event horizon location. (c) The proper distance Δs of an outgoing photon moving near the horizon is plotted against the Killing time t in logarithmic scale. The thick dashed line gives the results obtained using the backward surface method. The solid line labeled "analytic" gives the result obtained by integrating Eqs. (7)–(9) in text. The dotted line labeled "linearized" shows the trajectory given by Eq. (10). We see that the solid line and the dashed line are right on top of each other, with the dotted line just barely distinguishable. The inset shows the slope of all the lines being nearly 1/4, as given by Eq. (10). (d) The coordinate location of the horizon-containing region is shown as solid lines. A nonspherical initial trial surface is shown as a dashed line. The apparent horizon is shown as a dotted line. The nonspherical initial trial surface converges to the EH, just as do the spherical trial surfaces. The final horizon, at $t=0$, is shown as a thick line. (e) The evolution (at times $t=98.5M$, $t=98.4M$, $t=98.3M$, and $t=98.2M$ from top to bottom, with the line AH labeling the position of the true EH at $t=98.5M$) of a very distorted trial surface is shown in coordinate space. The evolution breaks down, showing that a highly distorted trial surface can develop trouble if the parameterization of the surface is unsuitable. See discussion in the text.

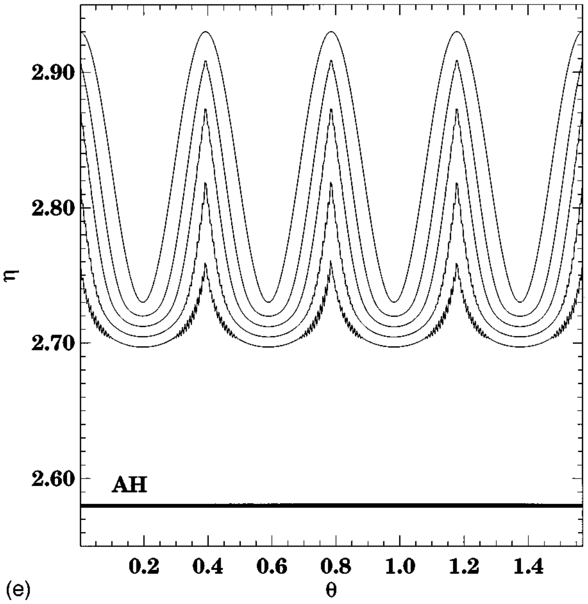

FIG. 2 (*Continued*).

$\alpha=0.7$, with (o) labeling the outer edge and (i) the inner edge of it. In Fig. 2(b), the radial coordinate r of the two surfaces (o) and (i) traced backwards in time is shown. At $t=100M$, the two surfaces are separated in the radial coordinate by $3.4M$. By $t=85M$, the two lines are separated by just one grid zone, corresponding to a difference in r of $0.35M$. By $t=70M$, the two lines are no longer distinguishable, with a separation down to 1/10th of a grid zone, a difference in r of $0.03M$. The separation exponentially decreases down to 1×10^{-6} grid zones at $t=0M$. This rapid shrinking of the horizon-containing region is a direct consequence of the divergence of null geodesics forward in time shown in Fig. 1. We conclude that if the aim is to locate the horizon to one grid zone accuracy, we have succeeded in doing so for the times $t=0M$ to $t=80M$. We emphasize that no information about the apparent horizon is used in the process.

For the purpose of comparison, in Fig. 2(b) we have also shown the trajectory of surfaces extremely far outside and far inside the horizon-containing region. These surfaces are shown as dashed lines. We see that the outer one converges quickly to the other test surfaces, while the inner one is initially trapped in a region of collapsed lapse. At $t=40M$, all the surfaces are practically indistinguishable.

In Fig. 2(c), we show that the convergence is in fact exponential. Here we plot, in the logarithmic scale, the maximum *proper* distance of a photon on the null surface (o) from the horizon, as a function of the Killing time t/M. The result is given by the thick dashed line. We get a straight line in the logarithmic plot, with a slope approaching 0.25, as shown in the inset. This is, as expected, the analytic value, as can be easily deduced in the following.

Consider a null trajectory in the Schwarzschild geometry near the horizon. The equations of motion are given by [17]

$$\left(\frac{dr}{d\lambda}\right)^2=\frac{1}{b^2}-\frac{1-\dfrac{2M}{r}}{r^2}, \tag{7}$$

$$\frac{d\phi}{d\lambda}=\frac{1}{r^2}, \tag{8}$$

$$\frac{dt}{d\lambda}=\frac{1}{b\left(1-\dfrac{2M}{r}\right)}, \tag{9}$$

where λ is an affine parameter and b is an integration constant. To leading order in $\epsilon=r-2M$, Eqs. (8) and (9) can easily be integrated to give

$$\epsilon=\frac{1}{b}e^{(t/4M)} \tag{10}$$

for an outgoing photon. Its maximum distance from the horizon is given by

$$\Delta s=\sqrt{\frac{2M}{b}}e^{(t/4M)}, \tag{11}$$

showing that the exponent is 1/4 in units of t/M. The trajectory given by Eq. (10) is plotted in Fig. 2(c) as the dotted line. It is just barely distinguishable from the solid line labeled as "analytic" in Fig. 2(c), which is the trajectory obtained by integrating the full null geodesic equation, Eqs. (7)–(9), without assuming $r-2M$ to be small. In turn the solid line lies right on top of the thick dashed line representing the numerical backwards surface method in the analytic spacetime, giving full support for the accuracy of the method, at least in this simple case.

In Fig. 2(d), we show the evolution of the coordinate locations of these surfaces in the first quadrant. The surfaces marked (i), (o), and AH are the same surfaces as shown in Fig. 2(b). Here, we have evolved an additional, nonspherical, surface. The location of this surface is given at $t=100M$ by the formula

$$\eta=\eta_0+A\cos w\theta, \tag{12}$$

with η_0 chosen to be the radial position of the apparent horizon, with $w=4$ and $A=0.2$. We evolve this surface to demonstrate that our initial trial surfaces need not have the same angular dependence as the EH (in this case, spherical). In a general dynamical black hole spacetime, it will not be possible to pick trial surfaces having the same coordinate or geometrical angular dependence as the EH to be traced out. Such trial surfaces are not necessary, though. In the case shown in Fig. 2(d), where the trial surface is quite nonspherical, with part of the surface inside and part outside of the EH, we see that the trial surface quickly converges when traced backwards in time. All of the surfaces are very close and almost completely spherical by $t=70M$. By $t=50M$, all the surfaces are within 1/10th of a grid zone. We note, however, that a sufficiently nonspherical surface may itself develop caustics, particularly if it is initially far from the true EH. In Fig. 2(e) we show the evolution (at times $t=98.5M$, $t=98.4M$, $t=98.3M$, and $t=98.2M$ from top to bottom, with the line marked AH labeling the position of the AH and thus the true EH at $t=98.5M$) of a highly distorted surface with the angular dependence of Eq. (12) increased to $w=16$, the amplitude decreased to $A=0.1$, and the center of

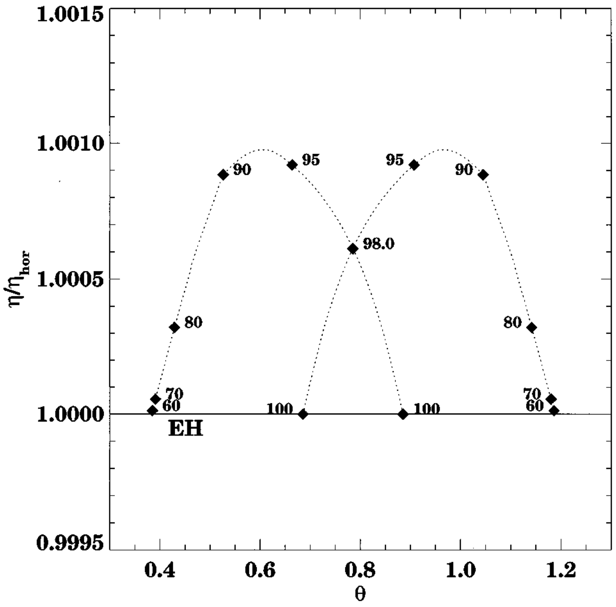

FIG. 3. To illustrate both the tangential drifting effect and in what sense the EH is attractive, as discussed in the text, we show the evolution of two photons launched at $t=100M$ right on the EH but with initial direction not exactly normal to the EH. They have a small but nonzero value in the ratio of the initial angular to radial coordinate velocities. The trajectories of the photons are represented by dotted lines and the times at various points on the trajectories are shown in units of M. The photons drift out from the horizon and cross each other at $t=98.0M$, producing a false horizon caustic point if these photons were taken as horizon generators. Tracing further backward in time, they turn around and asymptotically approach the correct radial location of the EH. The radial coordinate (vertical axis) is rescaled by the radial coordinate value of the EH, so that the EH is always at 1 on the vertical axis. The horizontal axis is θ in radians. Although the photons remain rather close to the correct EH location throughout the trajectory, they drift substantially in the tangential direction. For various implications of this behavior, see discussions in the text.

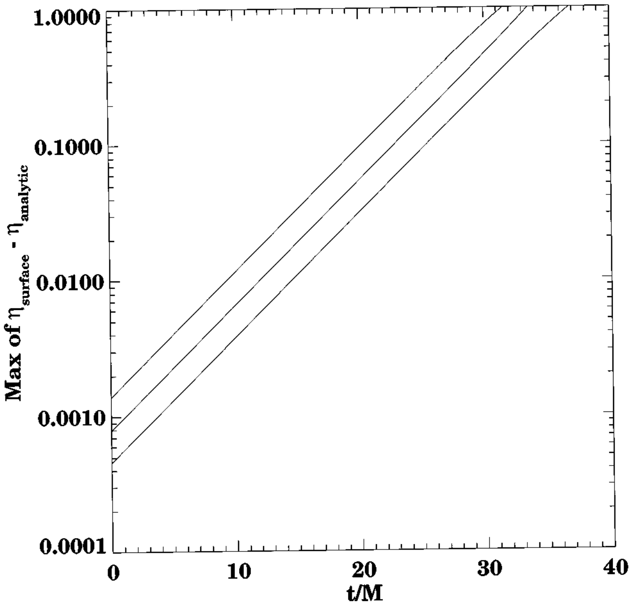

FIG. 4. We show the maximum coordinate separation between various trial surfaces and the exact horizon in the analytic Kerr spacetime with a rotation parameter $a/m=0.68$. The convergence to the exact solution is exponential, even though for a Kerr black hole rotating this rapidly the horizon has a very nonspherical geometry.

the perturbation moved away from the apparent horizon. We find that the surface method fails, with numerical noise developing as the surface tries to cross itself. This crossing in itself is not fatal to the surface method, but the particular parametrization (5) of the surface cannot describe this crossing. As we see below, the self-crossing of the surface can be handled with a proper parametrization, which is needed when *true* caustics develop, as in the collision of two black holes. We stress that when the black hole has returned to quasistationarity at late times, one does not expect the EH to have such a rapidly varying angular dependence and one would not pick such surfaces as the outer or inner boundaries of the horizon-containing region. We study such an extreme, contrived example only to explore the limits of our methods.

We note that at late times the data representing the spacetime itself as obtained in Refs. [20,14] become inaccurate due to the large spikes developing in the metric functions near the horizon [20]. As these spikes become ever steeper during the evolution, they become less and less well resolved, and therefore they are not accurately modeled on the numerical grid. This lack of accuracy in the spacetime itself is reflected in the calculation of the area of the apparent horizon at late times, which increases rather than remaining constant. Remarkably, this lack of accuracy at late times, when the EH finding algorithm is started, does *not* cause any difficulty in finding the EH at earlier times, as seen in the figures. Therefore, not only are our algorithms able to find accurately the true EH even with a poor initial guess for its location, they are also insensitive to inaccuracies in the spacetime data that inevitably occur at late times.

Finally, in Fig. 3, we show the tangential drifting that can occur with the backward photon method, as discussed in Sec. II. Figure 3 also serves as an illustration to the other comment we made above concerning the "attractiveness" of the EH to backward integrated photons, namely, the attraction is only in the global sense. In this example the tangential drifting is due to the choice of the initial direction of integration. Two photons are traced backward (shown as dotted lines) beginning at the exact location of the EH at $t=100M$, but with a 3% error in the starting direction. That is, instead of being normal to the EH ($p_\theta/p_r=0$, in obvious notation), we use $p_\theta/p_r=\pm 0.03$. In Fig. 3, the trajectories of these photons are shown with the corresponding times marked. The radial coordinates are normalized by the position of the EH, so that the EH is at 1 on the vertical (radial coordinate η) axis. We see that with the 3% error in the starting directions of the photons, the photons move out of the EH when traced backward in time. If these photons were taken as horizon generators, this would introduce a small error (note the scale of the η axis) in the location of the "EH" for a period of time, as the photons are gradually "attracted" back to the correct radial location after some integration. However, the error in the tangential direction is substantial, as we can see in Fig. 3, where the horizontal axis is given in terms of θ in radians. In particular, the two photons cross each other, creating an artificial "caustic" at $t=98.0M$ on their way out

TABLE I. For the case of the highly distorted nonrotating black hole, we find the normalized area of the EH at $t=0$. The normalized area is defined by $A=\text{area}/16\pi^2 M_{\text{ADM}}^2$. We find this quantity for a surface evolved with 25, 50, and 100 angular zones on the surface. We show the convergence order σ for the areas with varying numbers of angular zones. Thus we conclude that our method is second order convergent. We stress, however, that this numerical convergence is different from the physical convergence described in Sec. III.

Angular zones	Normalized mass
25	0.79612287
50	0.79572879
100	0.79563006
σ	1.99

from the EH. Although they return to the correct radial EH location eventually, their θ values change dramatically, making the trajectories very different from those of the true horizon generators.

2. Kerr spacetime

We briefly consider the Kerr spacetime, which is known analytically. In Ref. [15], the Kerr spacetime is studied in a coordinate system like that used for the studies of distorted Schwarzschild black holes discussed above. We have taken the analytic Kerr metric in these coordinates, with a rotation parameter $a/m=0.68$, to study our EH finders for rotating spacetimes where the EH location is known analytically. In Fig. 4 we show the maximum coordinate separation between three test surfaces and the analytically known horizon versus time. Again, we see an exponential convergence of the surfaces to the exact location, as expected. This is a confirmation both of our numerical implementation and of the physical convergence discussed above.

C. Numerical convergence

The final numerical issue to which we turn is that of convergence. Before beginning our discussion of numerical convergence we stress that *numerical* convergence is a subject entirely different from the *physical* convergence described in Sec. II. In that section we described how in a spacetime devoid of numerical error, the horizon-containing domain will shrink to zero size in exponential time. This is a consequence of the physical properties of the spacetime, and is true in the continuum and discretized spacetimes. It is this feature which allows us to locate accurately the EH in dynamical spacetimes.

Here we discuss the effect of resolution on our analysis of various spacetimes. This is a test of our numerical methods, in particular the interpolation and evolution schemes, not of the physical principles upon which our method is based. But it is an important test we routinely carry out for all our numerical studies.

Since we are taking our background spacetime as given, the numerical convergence of interest is the convergence of surfaces and surface quantities when the number of evolved points on the surface is changed. In essence, we are assuming the background spacetime to be given and interpolatable, and are concerned only with the convergence of the implementation of Eq. (4).

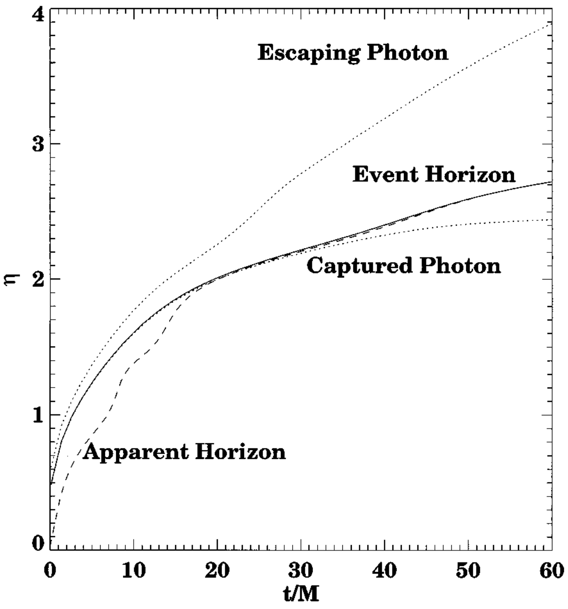

FIG. 5. The case of a spherical black hole with a massless scalar field falling in is shown. The dashed line represents the apparent horizon. The line marked "event horizon" is obtained by applying the backward methods to a point initially on the apparent horizon at $t=60M$. The dotted lines labeled "escaping photon" and "trapped photon" represent photons integrated forward in time from just outside and just inside the "EH."

Thus, to test convergence we trial surface and integrate this surface backwards using 25, 50, and 100 angular points on the surface using a given background spacetime. At $t=0$, we measure the normalized area of that surface (where the normalized area is defined as $A/16\pi^2 M_{\text{ADM}}$). As shown in Table I, this quantity is second order convergent with our integrator. These data are for the high amplitude case described below (the spacetime was computed on a 202×55 grid). This convergence is precisely what we would expect.

IV. DYNAMICAL SPACETIMES

A. Spherical distortions

The spherical case just discussed above was a vacuum Schwarzschild black hole with no true physical dynamics, although the motion of the coordinates through the spacetime makes both the black hole evolution and tracking of the EH nontrivial. In order to break the degeneracy between the AH and EH, we next consider a nonvacuum case. In this case we evolve a spherical black hole with a relativistic, massless Klein-Gordon scalar field falling into it. The system is described by the Klein-Gordon equation

$$g^{\mu\nu}\phi_{;\mu;\nu}=0, \tag{13}$$

coupled to the Einstein equation through the energy-momentum tensor of the scalar field. This problem has been studied previously in Ref. [20].

With a gravitating scalar field falling into the black hole, the system has true physical dynamics. Not only does the horizon move out as coordinates fall into the hole, as above, but now the horizon also expands in a geometric sense, as its area must increase to accommodate the infalling matter. A particular test case is shown in Fig. 5. Here the scalar field was set up in a Gaussian shell surrounding the black hole. As the field propagates into the hole, the horizon expands as expected. The solid line labeled "event horizon" is obtained by integrating the surface backward in time from the AH location at time $t=60M$. We refer to this line as the "EH" because as shown above it will converge rapidly to the true EH. The dashed line is the AH obtained by solving the AH equation [24] at each time slice. Note that the AH always lies inside the EH, as expected, and that at early times the EH is quite a bit larger as it starts expanding before the incoming matter arrives. The two solid lines labeled "escaping photon" and "trapped photon" were obtained by integrating radially outgoing null geodesics *forward* in time from locations 1/10th of a grid zone inside and four grid zones outside the EH at early times.

We note that even in this spherically symmetric case it is not possible to integrate accurately the path of the event horizon *forward* in time. Even when photons were placed right on the known horizon position initially, due to the unstable nature of the forward integration, the horizon could be tracked for only a short while before it would diverge away from the true EH. If we want to track the horizon further in time, one way is to "abandon" the original photons, and start new ones closer in to the horizon at the time when the original ones get too far apart, but the resulting horizon will consist of a discontinuous surface. A variation on this idea would be to use forward photons simply as a probe. If any photon integrated forward in time from a given point is not within the apparent horizon at late times, then that point may be considered outside the EH. By integrating many photons forward from many spacetime points, a horizon surface can be mapped out, as shown in Ref. [9]. This is an effective but time-consuming procedure, and the trajectories traced do not give the trajectories of the generators of the horizon.

B. Distorted axisymmetric black holes

Next we present results for an axisymmetric black hole that has been distorted by the presence of a gravitational wave. The initial data sets for these studies consist of an Einstein-Rosen bridge in the presence of a gravitational wave in the form originally considered by Brill, and have been described extensively in Ref. [25]. The gravitational wave is set up as a torus surrounding the black hole, and its location, amplitude, and shape can be varied essentially arbitrarily. The code used to evolve these data sets numerically has been discussed in Refs. [4,23,14].

The first case we study here is that of a black hole with a narrow ring of weak gravitational waves isolated from the hole initially. When this system is evolved, we expect the hole to become distorted slightly as the waves impinge on it, and then settle down to a Schwarzschild hole with a larger mass afterwards. Such a case provides a strong test of our methods as we must be able to track a horizon that begins essentially as a sphere, develops a distortion as it is hit by a nonspherical wave, and returns to a sphere after a long integration.

In Fig. 6(a), we demonstrate that we can locate the EH to high accuracy for such a spacetime. At time $t=75M$, the black hole has returned to approximately the Schwarzschild geometry. The apparent horizon, represented as the short dashed line in Fig. 6(a), has returned to an almost exact sphere. As the EH must lie outside the apparent horizon, the inner boundary of the horizon-containing region can be taken to be the location of the apparent horizon on the last time slice, $t=75M$. The outer boundary is taken to be the line marked (o) in Fig. 6(a), representing a spherical surface some distance outside the apparent horizon. The fact that this line is safely the outer boundary can be seen, as the area of this spherical surface is shrinking backward in time. On the other hand, the line marked (i) starting from the AH at $t=75M$ is expanding outwards. The two surfaces exponentially approach each other, and this separation becomes less than a grid zone at $t=62M$. Note that at this time, this one-grid-point-wide horizon-containing region is entirely outside the AH.

In Fig. 6(a), we also show other test surfaces as long dashed lines which are well outside or inside the horizon-containing region. All these test surfaces coincide to much less than 1/10th of the grid separation (corresponding to typical proper distances between the surfaces of less than $0.01M$) for the range $t=(0–40)\ M$. The inset shows an expanded view of the early time. All surfaces computed are shown, but they are completely indistinguishable in spite of their extremely different starting positions, clearly showing the power and stability of this method. For all practical purposes, this surface can be regarded as the EH. At $t=0$ the AH and EH practically coincide with each other. Then the EH foresees the coming of the wave and expands. As the wave is falling in, after about $t=15M$, the AH starts to expand and catch up. The behavior of the AH and EH is exactly as expected. (We note that the area of the hole continues to drift up after 40 M. This is a well-known numerical inaccuracy due to the development of a sharp peak in the radial metric component. This effect is in the background spacetime and is unrelated to our schemes for locating the horizon.)

In Fig. 6(b), we show the maximum separation over the whole surface between the outer and inner boundaries of the horizon-containing region versus time (maximum among the angular zones). The vertical axis is in terms of grid separation. As marked by squares, the maximum separation exponentially decreases down to 1, at $t=60M$, and then keeps decreasing to 1/10, 1/100, 1/1000, 1/10 000, and 1×10^{-5} of a grid zone by $t=50M$, $39M$, $27M$, $16M$, and $0M$, respectively. Again, for all practical purposes the outer and inner boundaries of the horizon-containing region coincide, and the region can be regarded simply as the location of the EH for earlier times. We also note that at $t=0$ for the present case, the EH surface is found to be geometrically spherical (using the tools described in the second paper in this series) to within 1 part in 10^6.

Finally, we also compare the result of our backward photon method to our surface method in Fig. 6(c). We show the coordinate location of the surfaces integrated directly according to Eq. (4) at various times, and also the location of surfaces formed by integrating the geodesic equation [Eq. (1)] backward in time. For the latter integration, the initial loca-

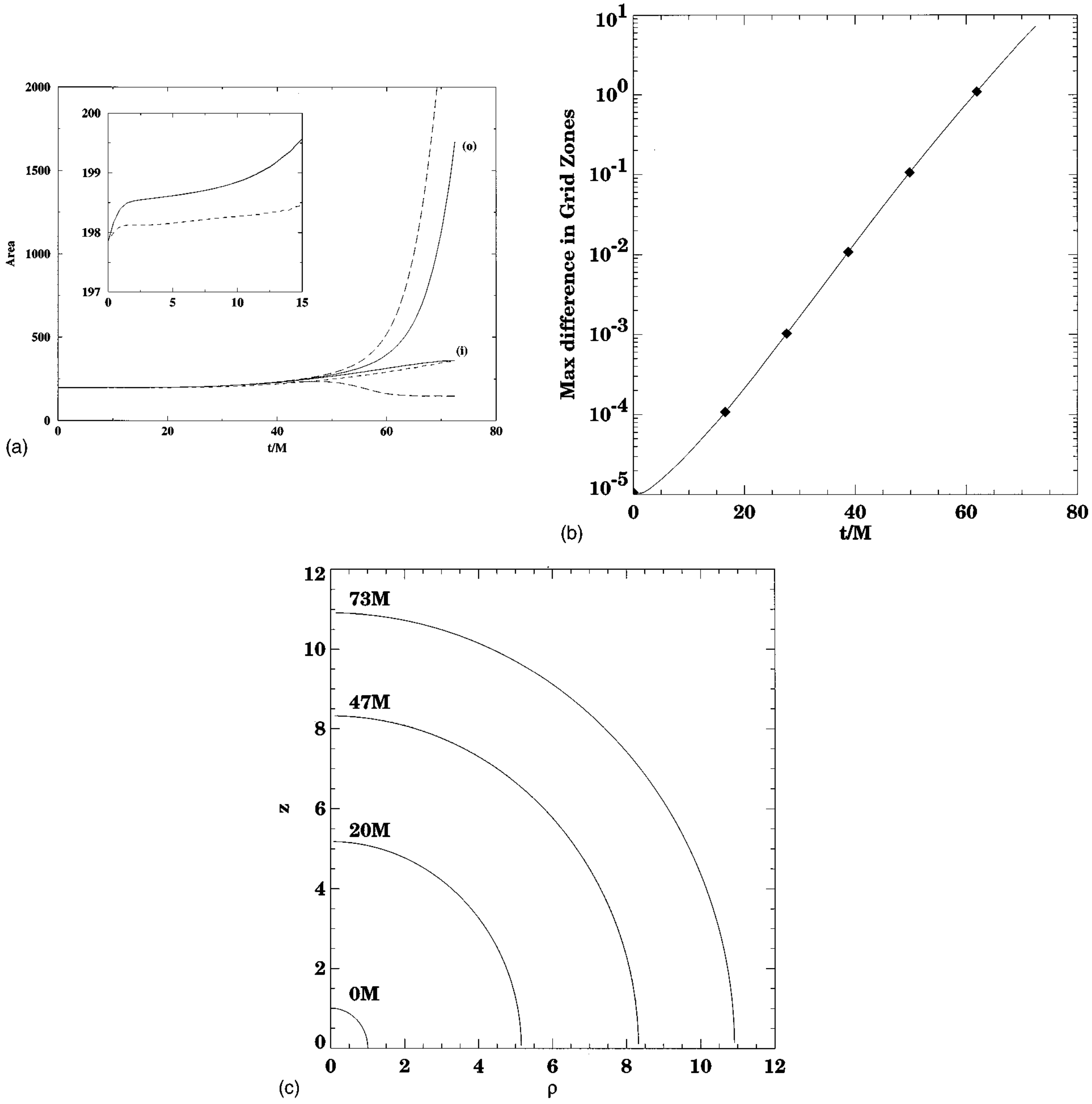

FIG. 6. (a) The area of various trial surfaces is shown for a slightly distorted Schwarzschild spacetime. The horizon-containing region [between the solid lines labeled (o) and (i)] is traced backward in time and compared to the area of the apparent horizon (short dashed line). Several other test surfaces are shown as long dashed lines. The attracting nature of the event horizon is dramatic, as all of the trial surface integrations trace the same path after some integration, although they start from very different initial locations. The inset shows an expanded view of the early time results. *All* surface integrations are shown, and are completely indistinguishable. (b) We show the maximum width among the angular zones of the horizon-containing region in the slightly distorted Schwarzschild spacetime, integrated backward in time. We note that the narrowing of the horizon-containing region is exponential. (c) We compare results obtained with the backward surface method to those obtained with the backward photon method for the perturbed Schwarzschild spacetime. The surface method results are shown as solid lines, while the surfaces formed by the backward integration of photons are shown as dashed lines. At all times, the results agree to within 0.05 grid zones, so that it is almost impossible to distinguish the results on this graph.

tions of the photons were taken from the initial trial surface, and their initial directions were taken to be normal to the surface. In this figure the results are indistinguishable, as they coincide to within 0.05 grid zones throughout the evolution. We note that we have also compared the results of the forward integration technique described in Ref. [9] to our backward methods. For this forward integration technique to determine the EH to similar accuracy as we have done here, however, would take around 10^5 times more CPU time than our backwards integration methods.

Next we briefly consider a more strongly distorted nonrotating black hole, providing a test of our methods in the more nonspherical and highly dynamic regime. In this case we choose initial data parameters $(Q_0, \eta_0, \sigma, n) =$

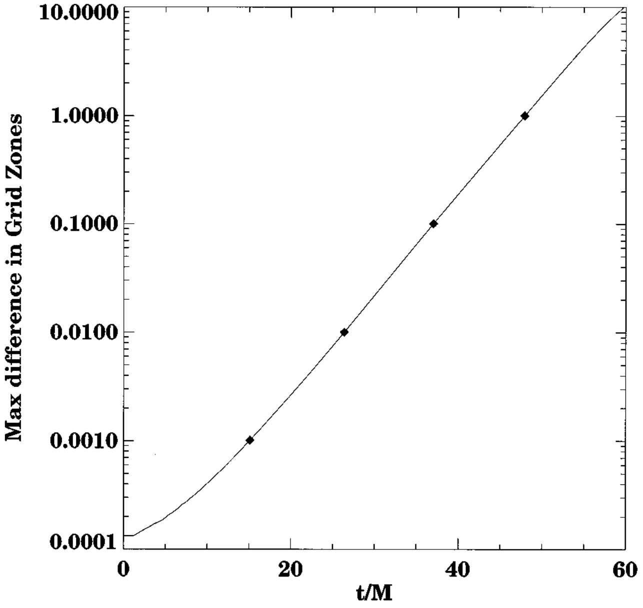

FIG. 7. We again show the width of the horizon-containing domain in terms of grid zones, here for the highly distorted single black hole. We note that the narrowing of this region is again exponential, diminishing by a factor of 10^5 from $t = 60M$ to $t = 0$.

(1.0,0,1.5,2) in the language of Ref. [24]. This black hole is significantly more distorted than the previous case (the ratio of the polar to equatorial circumference of the apparent horizon is 4.26 at the initial time). In Fig. 7 we show the maximum width of the horizon-containing region over all angular zones. The initial width of the horizon-containing region at $t = 60M$, chosen in the same manner as above, is ten grid zones. We see that this highly nonspherical case is no different from the previous cases. The width of the horizon-containing region decreases exponentially as a function of time, being less than one grid zone at $t = 48M$ and being only 0.0001 at $t = 0$. Again, we mark the points where the width of the region is 1/10, 1/100, and 1/1000 of a zone in the figure.

C. Distorted rotating black holes

The last single black hole cases we consider are rotating black holes. Rotating black holes are expected to be the end point of all astrophysical black hole systems, and so they are essential cases to be considered. Rotation adds a new dimension to the problem, as new metric elements are involved, another polarization of the gravitational wave is present, and horizon generators will now be dragged around the black hole due to its angular momentum. Furthermore, the horizon of a Kerr black hole is not spherical, but is oblate, with the oblateness related to the rotation parameter of the hole [26,27]. For these reasons the rotating case provides not only an important test bed, but also a rich area for the study of horizon dynamics.

We consider a distorted, rotating black hole data set evolved with a code described in Ref. [15]. In this case the black hole has been distorted by an axisymmetric gravitational wave, similar in construction to the distorted Schwarzschild black hole data sets described above. This particular data set corresponds to a dynamic rotating hole that evolves to a Kerr spacetime with a large rotation parameter of $a/m = 0.82$. In Fig. 8(a), we show the evolution of the coordinate locations of various test surfaces at various times. At $t = 60M$, the line marked (o) represents a coordinate sphere with an almost constant $\alpha = 0.7$. The surface marked (i) is approximately the late time apparent horizon. The

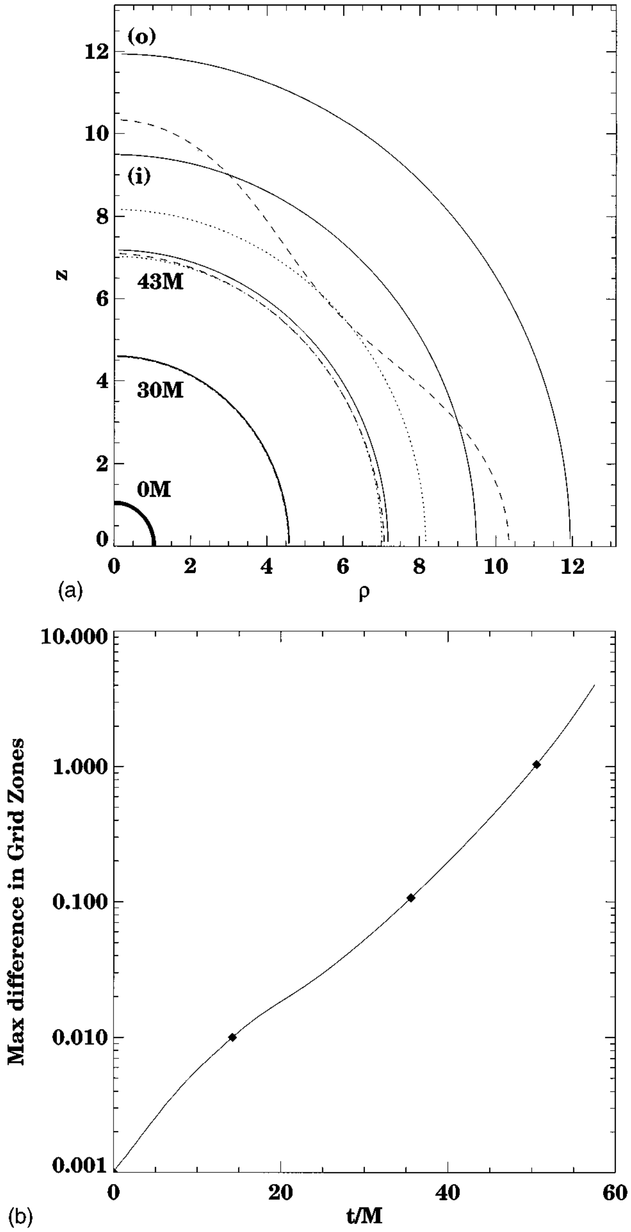

FIG. 8. (a) We show the coordinate locations for several trial surfaces for the distorted rotating black hole spacetime discussed in the text. The solid lines marked (i) and (o) represent the inner and outer edges of the horizon-containing region at $t = 60M$. A distorted trial surface and another trial surface initially inside the apparent horizon, shown as dashed and dotted lines, respectively, were also evolved. All four surfaces converge quickly to the same location. By $t = 43M$ all surfaces are very close to each other and by $t = 30M$ they are practically indistinguishable. The final location of all surfaces, denoting the horizon location at $t = 0$, is marked as a thick line. (b) We show the width of the horizon-containing region in terms of grid zones. We note that the separation exhibits the same exponential convergence as in the nonrotating cases.

horizon-containing region is bounded between these two surfaces marked (o) and (i). Other test surfaces, shown as dotted and dashed lines, are also evolved for comparison. We see that by $t=43M$ these surfaces have converged, and by $t=30M$ all the surfaces are essentially indistinguishable. In Fig. 8(b) we show the width of the horizon-containing region [maximum differences in grid zones between the two trial surfaces, (o) and (i)] as it diminishes exponentially. It is less than one grid separation by $t=50M$. Again, 1/10, 1/100, and 1/1000 of a grid zone separation are marked on the figure.

We note that although the coordinate shapes of these rotating black hole horizons are fairly spherical, their intrinsic geometries are highly distorted. For an analytic Kerr spacetime, if the rotation parameter exceeds a critical value of $a/m=0.867$, the horizon geometry becomes so distorted that it cannot be embedded into a Euclidean space [26,15]. When a gravitational wave is also present in the system, the horizon geometry becomes more distorted and evolves in time. Therefore, the cases presented here, with rotation parameters of $a/m=0.68$ (Fig. 3) and $a/m=0.82$ [Figs. 8(a) and 8(b)] have highly nontrivial horizon geometries, and our horizon finder converges to the true horizons quickly and tracks them very accurately. The geometry and physics of the EH will be analyzed in the third paper in this series [12].

D. Colliding black holes

In this section we focus on extracting the event horizon from data representing the collision of two equal-mass black holes. The discussion here considers the evolution of the Misner vacuum black hole spacetime [28], but the methods discussed apply equally well to black holes formed from matter collapse as discussed in Refs. [29,9,8]. The evolution of the Misner spacetime itself has been treated extensively in a series of papers [5,30,31], and we will not go into the details of those calculations here. As we discussed in Sec. II above, both the backward surface and photon methods can be used to study horizons in the collision of two black holes. We use these techniques here to find the EH for the two black hole spacetime parametrized by the quantity $\mu=2.2$, corresponding to two black holes separated initially by a proper distance of $L=8.92M$. We also note that due to the nature of the Cadez coordinates in which the evolution takes place, we can still use the parametrization described in Eq. (5). (See Ref. [31] for definitions of these parameters and the Cadez coordinate system.)

In Figs. 9(a)–9(c) we show results of integrating the boundary surfaces of the horizon-containing region backward in time, starting at a late time $(t=75M)$. At this time the two holes have already coalesced, forming a single, larger, almost stationary, black hole. As the AH is readily found in this case, we can use it as the inner boundary of the horizon-containing region. In Fig. 9(a), the lapse at $t=75M$ is shown in a 2D ρ-z coordinate plot. The surface marked (i) coincides with the AH at final times. The lapse on the AH has a nearly constant value $\alpha=0.34$. The distribution of the lapse is basically spherical at this late time, signaling that the geometry is approaching that of Schwarzschild. (It is basically Schwarzschild except in the innermost part where the lapse is practically zero. Notice that one of the throats, where the lapse is exactly zero, can be seen on the z axis.) Again, the outer boundary of the horizon-containing region, denoted (o), is taken to be a sphere of almost constant $\alpha=0.7$. In Fig. 9(b), the evolution of the surfaces at various times is shown. The (i) and (o) surfaces are indistinguishable even at $t=50M$. To show the convergent effect more clearly, again we show a highly nonspherical surface as a short dashed line. From $t=40M$ backwards, all lines are indistinguishable.

In Fig. 9(c), the maximum width of the horizon-containing region between surfaces (i) and (o) in terms of grid separation is plotted versus time, with the points of 1/10, 1/100, 1/1000, 1/10 000, and 1/100 000 of a grid zone separation marked. If the aim is to locate the EH to one grid separation, we have achieved that in the range $t=(0–58)$ M, fully covering the epoch of interesting dynamics of the coalescence of the two black holes. (It also covers more than thrice the dynamical time scale of the final system, as the natural period of the final black hole is $16.8M$).

As discussed in Sec. II, some implementations of the backward surface method may require special treatment on the axis of symmetry. There is a caustic point that must develop where the horizon surface intersects the z axis. At this point a cusp develops in the horizon, causing its normal to become discontinuous. This means that the surface can hit the z axis at an angle, as one can see clearly in Fig. 9(b) for the surface marked $t=0$ (i.e., the EH is not perpendicular to the axis on the line between the holes.) Because of the symmetry involved in this problem, we know in advance where this happens, and so it is easy to devise a numerical treatment to handle this special situation. In evolving Eq. (4) one requires derivatives of the surface. These derivatives are well defined everywhere except at the caustic point on the z axis, where only one-sided derivatives are defined. In practice we find that in numerical evolution of the surface one can use a uniform treatment of one-sided derivatives all along the boundary, including both the equator and the z axis where the cusp develops.

In Fig. 10 we show a comparison of using backwards geodesic integration and the backwards surface method described above. It is clear that the backwards surface method and backwards photon method give the same result, agreeing to within 0.05 grid separations throughout the calculation. As these methods are completely independent, sharing only the spacetime data to which they are applied, in each case they confirm that the horizon has been accurately found, even at the caustic point.

As we discussed in Sec. II, by considering the entire set of null rays generating the horizon surface, including those that have not yet joined the horizon, one can also treat this problem using the backward surface method in a way that does not require any special treatment at the cusp. We allow the surface to pass through itself going backwards in time where the caustic line forms [21]. In this way we can trace out the set of generators that will join onto the horizon in the future.

However, when the locus of generators is included in the evolution, the parametrization given by Eq. (5) is not suitable as it may become multiply valued. The evolution equation of the surface method [Eq. (4)] gives no restriction on the parametrization. We choose to integrate the surface in cylindrical ρ-z coordinates in this case, choosing

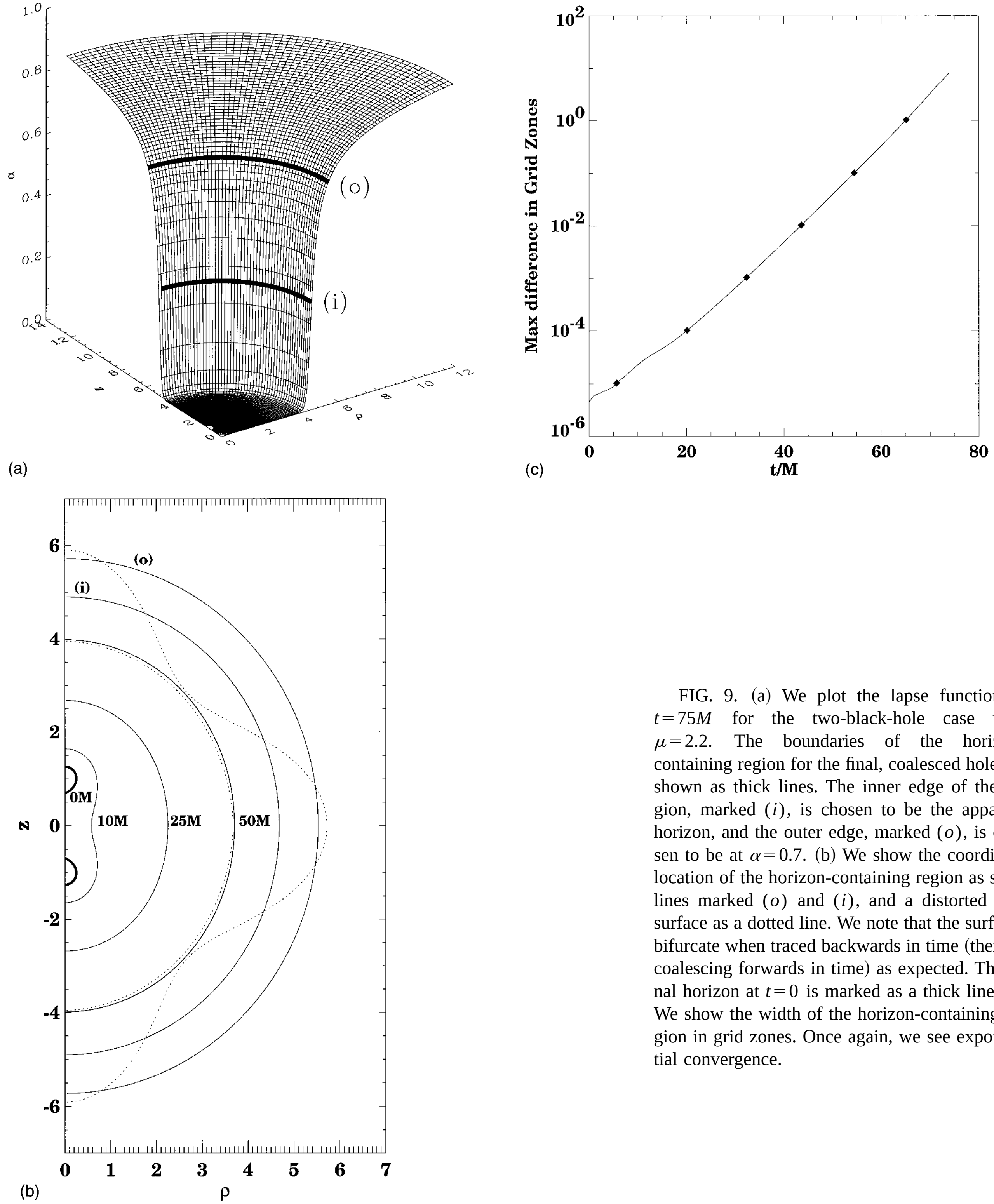

FIG. 9. (a) We plot the lapse function at $t=75M$ for the two-black-hole case with $\mu=2.2$. The boundaries of the horizon-containing region for the final, coalesced hole are shown as thick lines. The inner edge of the region, marked (i), is chosen to be the apparent horizon, and the outer edge, marked (o), is chosen to be at $\alpha=0.7$. (b) We show the coordinate location of the horizon-containing region as solid lines marked (o) and (i), and a distorted trial surface as a dotted line. We note that the surfaces bifurcate when traced backwards in time (thereby coalescing forwards in time) as expected. The final horizon at $t=0$ is marked as a thick line. (c) We show the width of the horizon-containing region in grid zones. Once again, we see exponential convergence.

$$f(z,\rho,t)=\rho-s(z,t), \tag{14}$$

as the surface is single valued in z.

In Fig. 11 we show the locus of generators as it is evolved by the code. The locus of generators clearly passes the origin and continues smoothly across the z axis. As the surface possesses a rotational symmetry about the z axis, it is self-intersecting where it crosses $\rho=0$. These self-intersection points are physical caustic points. The horizon and locus clearly show the cusplike nature of the horizon at the caustic point. With the parametrization described in Eq. (14), no special treatment is needed for handling the caustic point.

In Fig. 12 we show the initial horizons surrounding the throats with their cusps facing each other, and the entire surface of all photons that will ever join the horizon surface for the full evolution to the future. This remarkable picture adds to our understanding of the location of the EH of this classic

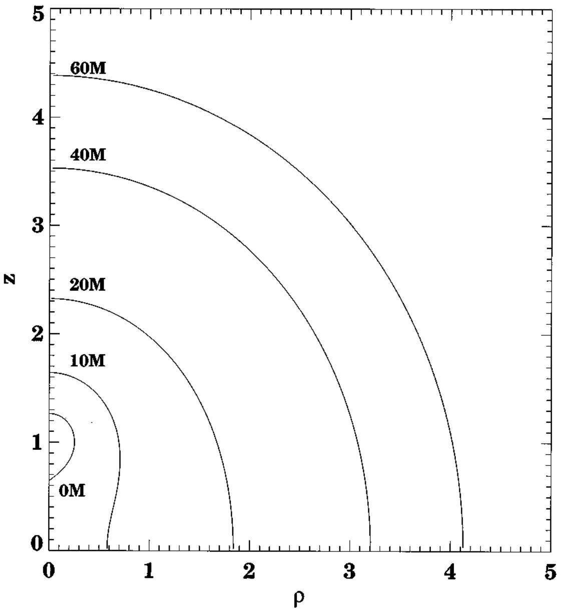

FIG. 10. The event horizon for the collision of two black holes is computed by two different methods. The solid lines show the result of integrating a trial surface backward in time (starting at the position of the apparent horizon), and the dashed lines show the surfaces obtained by directly integrating the geodesic equation for a series of backward photons starting at the same location and aimed normal to the apparent horizon surface. Geodesics which leave the horizon through caustics are not displayed. The results agree to within 0.05 grid zones throughout, making it almost impossible to distinguish between the solid and dashed lines.

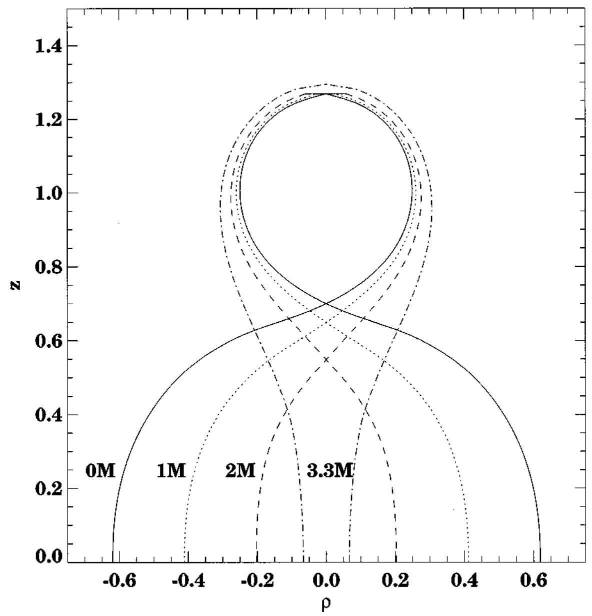

FIG. 11. Here we show the evolution of the event horizon and locus of generators of the $\mu = 2.2$ two-black-hole collision. Only the top half of the system, containing one hole, is shown. The first surface at $t = 3.3M$ shows a single, elongated black hole. The evolution of the surface is displayed at $t = 2M$, $t = 1M$, ending at $t = 0$. By $t = 2M$, the surface has already crossed itself, showing two separate holes and the locus of generators that have not yet joined the horizon. The cusp points where the surface intersects itself are caustics of the horizon.

two-black-hole initial data set discovered by Misner [28] over 30 years ago.

V. CONCLUSIONS

We have developed a powerful method for finding black hole event horizons in dynamic spacetimes based on the ideas of (i) backward integration and (ii) integrating the entire null surface. This opens up the possibility of studying the dynamics of event horizons in numerical relativity.

Our methods allow the determination of the horizon location to exceptional accuracy, even in highly distorted dynamical black holes involving strong gravitational waves, rapidly rotating black holes, and colliding black holes. Because of the convergence properties of null surfaces when integrated backwards, the horizon-containing region can be narrowed to resolutions far better than that of the numerical simulation which created the background spacetimes. The width of the horizon-containing region diminishes exponentially in time. We showed that this empirical result is expected by an analysis of static spacetimes. Thus, the event horizon can be located to a very small fraction of the grid spacing.

We have shown that if the spacetime can be evolved to a point that the black hole has returned to approximate stationarity, a horizon-containing region can be chosen. The precise width of this region is unimportant, as it exponentially decreases backwards in time. In particular, our methods do not require knowledge of the apparent horizon, and so they

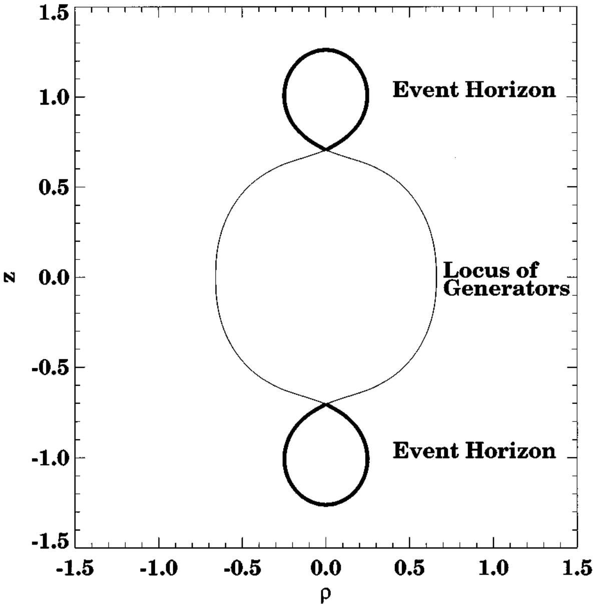

FIG. 12. The coordinate location of the event horizon (thick line), and the locus of generators (thin line) that have not yet joined the horizon, is shown at time $t = 0M$ for two black holes colliding head on. The z coordinate line marks the symmetry axis. This locus of generators will join the horizon through the point where the surface intersects itself.

should be a useful tool for analyzing spacetimes even in cases where the apparent horizon cannot be found (e.g., if the time slicing does not intersect the apparent horizon). The impact of this development on the numerical investigations of the cosmic censorship conjecture and the hoop conjecture could prove interesting.

Our methods allow one to locate and trace the actual generators of the event horizon, as well as its location in spacetime. The methods are also able to handle caustic points on the horizon surface. The ability to find horizons and their generators accurately and efficiently allows one to probe geometrical and physical properties of the horizon, including horizon oscillations, generators, membrane-paradigm-type quantities, and other previously unattainable physical properties. The methods for finding these quantities will be the topic of the second paper [11] in this series. These tools will be important for studying the structure of event horizons in dynamical black hole spacetimes, including colliding black holes, as we will present in the third paper in this series [12].

ACKNOWLEDGMENTS

We are most grateful to Kip Thorne for many discussions and for contributing ideas to this work. We thank Richard Isaacson and Richard Matzner for useful discussions. We also thank Scott Hughes, Charles R. Keeton II, Stuart Shapiro, Saul Teukolsky, and Kevin Walsh for allowing us to use the Cornell code for making comparisons with our code, and especially S.H., C.R.K., and K.W. who, together with one of us (P.W.), developed some of the input-output (I/O) routines used in the present version of our code. We are grateful to Pete Anninos for help with the two-black-hole studies, and to Steve Brandt for providing data for evolved rotating black holes that were discussed in this paper. J.M. acknowledges financial support from Ministerio de Educación y Ciencia of Spain. This research is supported by the NCSA, the Pittsburgh Supercomputing Center, and NSF Grants Nos. PHY91-16682, PHY94-04788, PHY94-07882, and PHY/ASC93-18152 (ARPA supplemented).

---

[1] A. A. Abramovici *et al.*, Science **256**, 325 (1992).
[2] E. Seidel and W.-M. Suen, Int. J. Mod. Phys. C **5**, 181 (1994).
[3] C. Bona and J. Massó, Int. J. Mod. Phys. C **4**, 883 (1993).
[4] A. Abrahams, D. Bernstein, D. Hobill, E. Seidel, and L. Smarr, Phys. Rev. D **45**, 3544 (1992).
[5] P. Anninos, D. Hobill, E. Seidel, L. Smarr, and W.-M. Suen, Phys. Rev. Lett. **71**, 2851 (1993).
[6] S. W. Hawking and G. F. R. Ellis, *The Large Scale Structure of Spacetime* (Cambridge University Press, Cambridge, England, 1973).
[7] P. Anninos, D. Bernstein, S. Brandt, J. Libson, J. Massó, E. Seidel, L. Smarr, W.-M. Suen, and P. Walker, Phys. Rev. Lett. **74**, 630 (1995).
[8] R. Matzner, E. Seidel, S. Shapiro, L. Smarr, W.-M. Suen, S. Teukolsky, and J. Winicour, Science **270**, 941 (1995).
[9] S. Hughes, C. R. Keeton II, P. Walker, K. Walsh, S. L. Shapiro, and S. A. Teukolsky, Phys. Rev. D **49**, 4004 (1994).
[10] *Black Holes: The Membrane Paradigm*, edited by K. S. Thorne, R. H. Price, and D. A. Macdonald (Yale University Press, London, 1986).
[11] J. Massó, E. Seidel, W.-M. Suen, and P. Walker (in preparation).
[12] J. Massó, E. Seidel, W.-M. Suen, and P. Walker (in preparation).
[13] R. Gomez, P. Papadopoulos, and J. Winicour, J. Math. Phys. **35**, 4184 (1994).
[14] D. Bernstein, D. Hobill, E. Seidel, L. Smarr, and J. Towns, Phys. Rev. D **50**, 5000 (1994).
[15] S. Brandt and E. Seidel, Phys. Rev. D **52**, 870 (1995).
[16] P. Anninos, G. Daues, J. Massó, E. Seidel, and W.-M. Suen, Phys. Rev. D **51**, 5562 (1995).
[17] C. W. Misner, K. S. Thorne, and J. A. Wheeler, *Gravitation* (W. H. Freeman, San Francisco, 1973).
[18] E. Seidel and W.-M. Suen, work presented in a talk at the 6th Gregynog Workshop (unpublished).
[19] J. Libson, in proceedings of the Numerical Relativity Conference, edited by P. Laguna (unpublished).
[20] E. Seidel and W.-M. Suen, Phys. Rev. Lett. **69**, 1845 (1992).
[21] We thank Kip Thorne for this idea.
[22] W. H. Press, B. P. Flannery, S. A. Teukolsky, and W. T. Vetterling, *Numerical Recipes* (Cambridge University Press, Cambridge, England, 1986).
[23] P. Anninos, D. Bernstein, D. Hobill, E. Seidel, L. Smarr, and J. Towns, in *Computational Astrophysics: Gas Dynamics and Particle Methods*, edited by W. Benz, J. Barnes, E. Muller, and M. Norman (Springer-Verlag, New York, 1994).
[24] P. Anninos, D. Bernstein, S. Brandt, D. Hobill, E. Seidel, and L. Smarr, Phys. Rev. D **50**, 3801 (1994).
[25] D. Bernstein, D. Hobill, E. Seidel, and L. Smarr, Phys. Rev. D **50**, 3760 (1994).
[26] L. L. Smarr, Phys. Rev. Lett. **30**, 71 (1973).
[27] S. Brandt and E. Seidel, Phys. Rev. D **52**, 856 (1995).
[28] C. Misner, Phys. Rev. **118**, 1110 (1960).
[29] S. L. Shapiro and S. A. Teukolsky, Phys. Rev. D **45**, 2739 (1992).
[30] P. Anninos, D. Hobill, E. Seidel, L. Smarr, and W.-M. Suen, Technical Report No. 24, National Center for Supercomputing Applications (unpublished).
[31] P. Anninos, D. Hobill, E. Seidel, L. Smarr, and W.-M. Suen, Phys. Rev. D **52**, 2044 (1995).